Figure 6. Expression of brain-derived neurotrophic factor (BDNF), nerve growth factor (NGF) and macrophage antigen (Mac)-2 correlated to the phenotype of activated microglia/macrophages and increased spinal cord compression in *twy/twy* **mice.** Immunofluorescence staining for the expression of BDNF, NGF, and Mac-2 (red) colocalized with iNOS and arginase-1 (green) in the anterior column of 12- (A), 18- (B) and 24-week-old (C) *twy/twy* mice (n = 5 for each time point). The expression levels of neurotrophic factors and Mac-2-positive cells increased with the worsening of spinal cord compression. Neurotrophic factor and Mac-2 colocalized with arginase-1- and CD206-positive cells (arrow heads), but not with iNOS- and CD16/32-positive cells. Scale bars = 50 μm. A–C microphotographs were taken using confocal laser scanning microscope.
doi:10.1371/journal.pone.0064528.g006

number of remaining surviving neurons when the transverse remnant area of the spinal cord of the *twy/twy* mouse spinal cord decreased to ≤70% of the control (+/*twy* mice) [33], and further that the extent of demyelination and Wallerian degeneration in the white matter increased proportionately with the magnitude of spinal cord compression [35]. We also reported a significant increase in TUNEL-positive cells in the anterior horn and also glial cells in the white matter, in spinal cord segments located rostral and caudal to the segment with maximal compression [8]. It is well-known that activated microglia/macrophages secrete cytotoxic substances including various cytokines (e.g., TNF-α, IL-1 and -6), reactive free radicals, and nitric oxide. In addition, the major role of microglia at the lesion centre is probably rapid phagocytosis of debris [25,40]. Our results suggest that neuronal loss through the mechanisms of necrosis and apoptosis is associated with activation of microglia/macrophages, production of proinflammatory cytokines by these cells, and putative phagocytosis, which may also be associated with axonal demyelination in the *twy/twy* spinal cord. This chain of events is somewhat similar to the delayed apoptosis of oligodendrocytes following activation of microglia after SCI [41].

As part of the response to chronic and progressive spinal cord compression, the present results showed high numbers of CD11b-positive cells, representing resting and activated microglia, as well as recruited macrophages, at different stages of microglia/macrophages activation and polarization [29]. The proportion of both M1 and M2 microglia/macrophages increased with the severity of spinal cord compression with abundant cells appearing as the M2 phenotype at 24 weeks in *twy/twy* mice. Furthermore, the results also showed increased M1/M2 antigen expression rate, a ratio known to correlate with CNS damage and repair [22]. M2 microglia/macrophages seem to promote neuroprotection, neurogenesis, and repair even in severely compressed spinal cord. On

the other hand, further progression of the spinal cord compression may have resulted in the induction of CD11b -positive cells into the M1 phenotype, which is known for its deleterious effects [27]. We reported previously the presence of axonal and dendritic outgrowth, which were induced by overexpression of neurotrophic factors at the site of compression in the *twy/twy* mice spinal cord [36]. Immunostaining in the present study demonstrated high co-expression of neurotrophic factors in M2 phenotype macrophages as well as increased expression of Mac-2, which reflects enhanced phagocytic activity [40,42]. These changes possibly represent the spinal cord response to chronic progressive spinal cord compression in order to maintain neuronal function [28,36].

The results of flow cytometry provided further details on the phenotypes of the involved cells, where resting microglia mainly expressed M2 markers, as described previously by other groups [17,32]. Our data confirmed that resting microglia are also the source of activated microglia/macrophages, since the population of resident microglia decreased while that of the activated microglia/macrophages increased in response to severity of spinal mechanical compression. In addition, the phenotypic changes in activated microglia/macrophages showed dynamic behavior with important M2 phenotype populations in 18- and 24-week-old *twy/twy* mice and further increase in the M1 phenotype at 24 weeks, probably reflecting worsening of chronic spinal cord compression. The results related to the serial changes in the expression levels of phenotypic markers in activated microglia deserve special attention. It has already been documented both *in vitro* and *in vivo* that resting microglia possesses the M2 phenotype and are the only neural cells that express arginase-1 [26,32]. However, after their activation, these cells express different markers in a time-related manner. For example, arginase-1 is a well-documented early marker expressed in those cells that undergo the alternative pathway of activation to acquire the M2 macrophage phenotype,
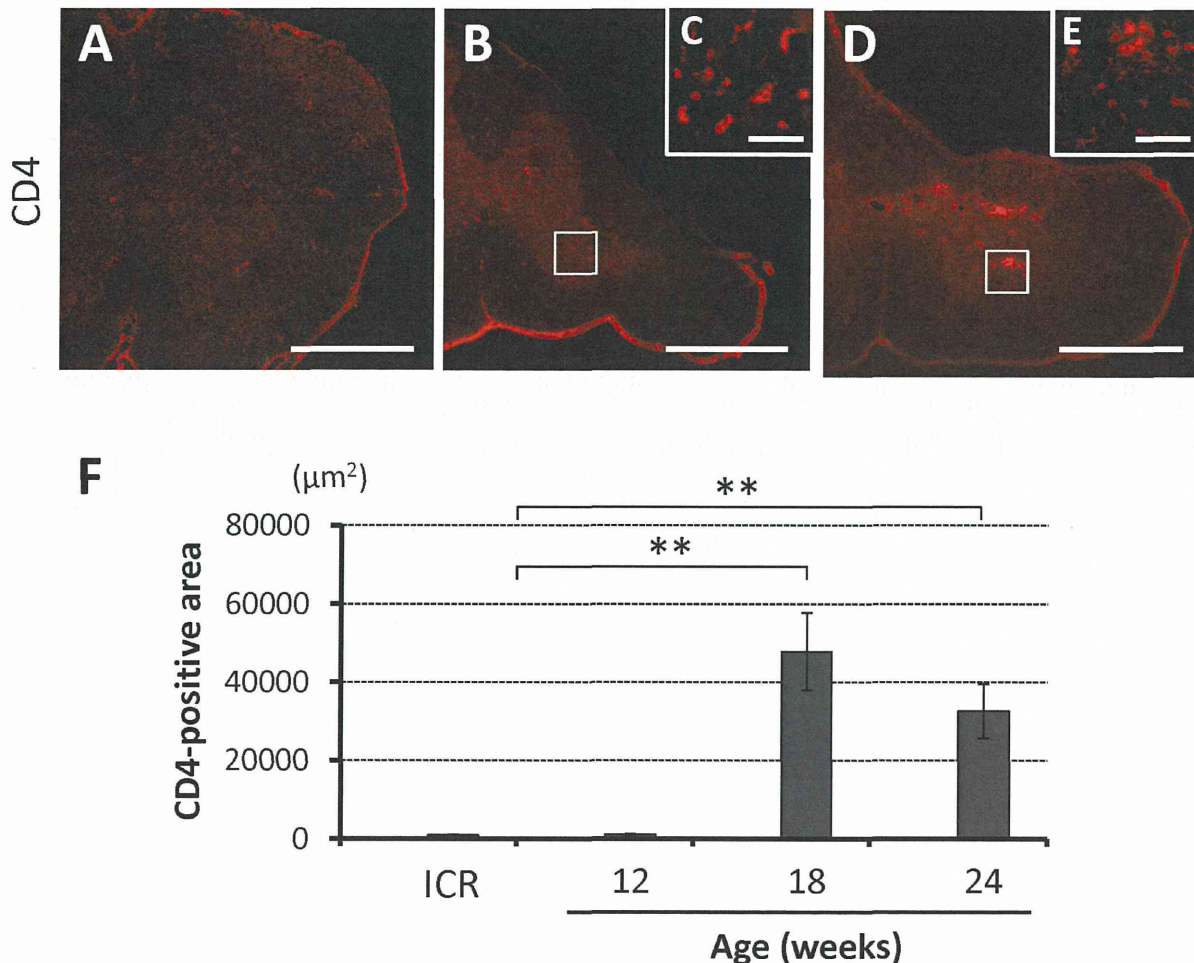
Figure 7. The prevalence of CD4-positive cells in the spinal cord of *twy/twy* **mice.** Immunostaining of infiltrating helper T cells increased with the worsening of spinal cord compression, especially in 18-week-old *twy/twy* mice (A–E). Panel (C) and (E) are high-power photographs of the anterior horn (boxed area). (F) CD4-positive area in control ICR, 12-, 18-, and 24-week-old *twy/twy* mice. Scale bar = 500 μm (A, B, D); 200 μm (C, E). Data are mean±SD. **p<0.01 (n = 3 for each time point).
doi:10.1371/journal.pone.0064528.g007

whereas iNOS is a marker of cells activated through the classical pathway, changing into M1 activated macrophages [22]. As the activation process advances, the fully mature activated cells express CD16/32 and CD206, which are phenotypic hallmarks of M1 and M2 macrophages, respectively [17,28]. Our immuno-histochemical and flow cytometric data showed a similar behavior where the expression of such phenotypic markers increased with time, representing completion of the macrophage activation process. CD206 is an endocytic receptor that recognizes glyco-protein for antigen processing and presentation and is widely used to identify the M2 phenotype [26]. Our results showed that the expression of iNOS and arginase-1 persisted and increased with time; possibly related to the persistence of the insult triggering microglial/macrophages activation, since these markers mainly reflect the early stages of activation [22].

Cells that were double immunopositive for M1 and M2 phenotypic markers were seen locally within the spinal cord, which is highly suggestive of microglia/macrophages undergoing phenotype change due to environmental influences created by the cervical compression. Polarization of the microglia/macrophages requires an active response in the form of inflammatory cytokines, other immune effector molecules and neurotrophic factors released from the cells in the injured tissue as well as from

different cells recruited to the site of the primary insult [27]. The sources of these cytokines remain controversial. Astrocytes seem to be the main source of TNF-α since they are the most abundant cell type after SCI capable of producing this cytokine [43]. Previous studies indicated that the main source of IFN-γ is blood-derived cells recruited to the site of injury (macrophages, natural killer cells, neutrophils and helper T cells) through the inflammatory process mediated by some ILs [44,45]. Some of these recruited cells can produce Th2 cytokines, but the main source of IL-4 and IL-13 seems to be microglia [46,47]. However, the pathophysi-ology of chronic spinal cord compression in the *twy/twy* mouse spinal cord could include a limited blood cell access into the injured spinal cord, and there is no evidence of the destruction of the blood spinal cord barrier [33,35,37], thus limiting the infiltration of helper T cells and neutrophils. Under such circumstances, the expression of IFN-γ is expected to be weak and TNF-α becomes the most important Th1 cytokine responsible for macrophage activation. The preserved blood spinal cord barrier would also limit the supply of Th2 cytokines; leaving resting and activated microglia at the injury site as the main source of Th2 cytokines for alternative activation of microglia/macro-phages [46,47]. While there is no evidence to our knowledge of disruption of the blood spinal cord barrier in the *twy/twy* mouse to
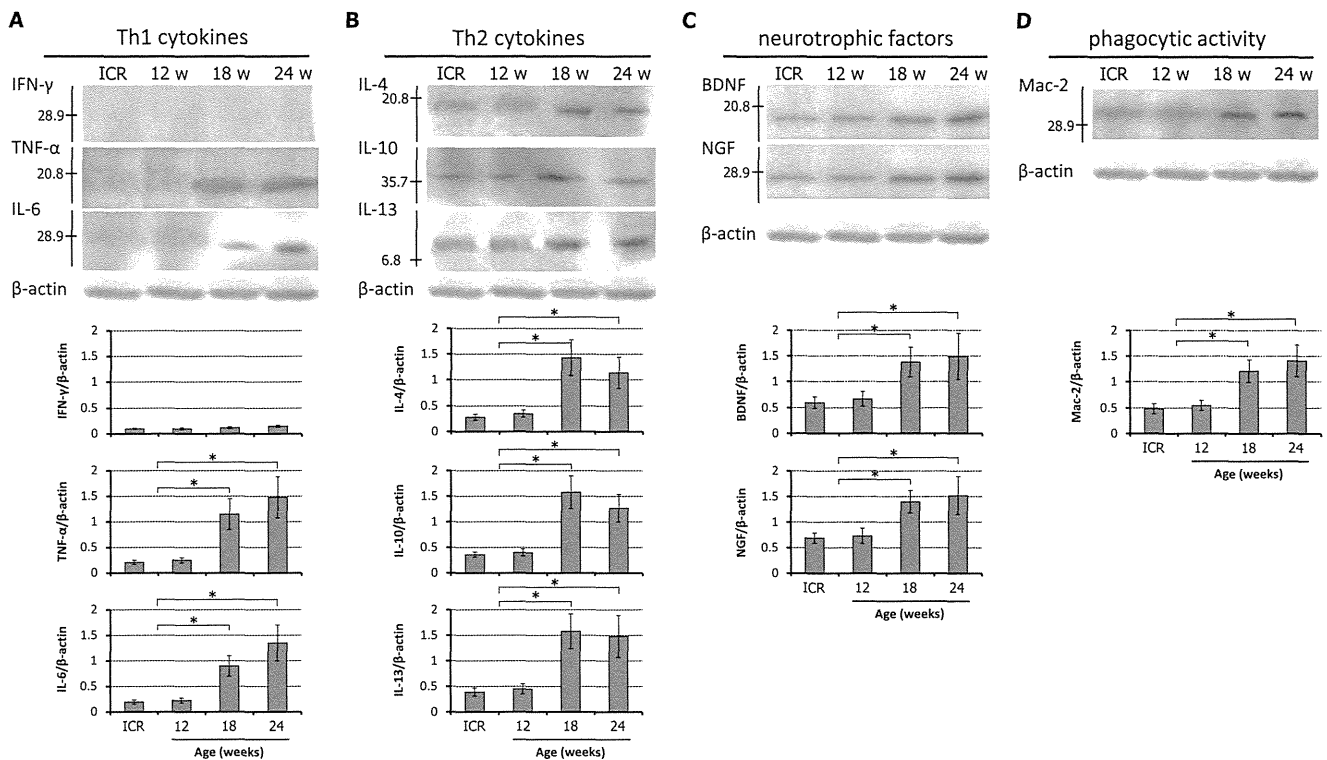
Figure 8. Cytokine expression and phagocytic activity in the *twy/twy* mouse. Immunoblot analysis of T helper 1 (Th1), T helper 2 (Th2) cytokines, neurotrophic factors and phagocytic activity in control ICR, 12, 18, and 24-week-old *twy/twy* mice. (A) The expression of IFN-γ was not detected in all age groups, but the expression levels of TNF-α and IL-6 increased significantly with the severity of spinal cord compression. (B) The expression levels of Th2 cytokines were highest in 18-week-old and remained significantly elevated in 24-week-old *twy/twy* mice. (C) The expression levels of neurotrophic factors and Mac-2 (D) increased significantly with the severity of spinal cord compression. Each graph shows the relative band intensity normalized to that of β-actin. Data are mean±SD. *p<0.05 (n = 3 for each time point).
doi:10.1371/journal.pone.0064528.g008

date, future research may prove otherwise. For analysis of this aspect, special *twy/twy* background chimeric mice models would be required [42], which are not currently commercially available; therefore, the possibility of cytokines deriving from blood and having an important role in determining inflammatory and immunomodulatory activity within the spinal cord remains as a possible limitation of our animal model. Our immunoblot results provided insight on the polarization process; the expression of Th2 cytokines increased from 18 weeks in possible correlation with the enlarged activated microglia population. The transient increase of Th2 cytokines explains our findings of M2 phenotype being the predominant type of activated cell; which would also explain the enhanced expression of neurotrophic factors and Mac-2 [19,26,29]. The present results also demonstrated increased expression of Th1 cytokines, as reported previously by our group [8], together with the reported increase in IL-6 expression as part of the inflammatory process [42,48]. Thus, over-expression of TNF-α in the *twy/twy* mice may be the most important Th1 cytokine responsible for M1 macrophage activation [28].

Interestingly, the resultant increase in the neurotropic factors at the site of spinal cord compression did not reverse the pathological changes of increased expression of proinflammatory cytokines and apoptosis of neurons and glia. Accordingly, the only treatment available at present is the surgical removal of the cause of chronic spinal cord compression [1–4]. However, surgery is unlikely to reverse the symptoms in patients with advanced cervical compressive myelopathy. In such patients, the use of specific antibodies against Fas ligand to reduce apoptosis of neurons and

oligodendrocytes [7,37], promotion of neuronal regeneration, through blockade of the inflammatory cascade, and induction of the M2 phenotype [48] are promising options for combined medical therapies in future management of this condition.

In conclusion, the present study demonstrated that chronic and progressive spinal compression induced over-expression of Th1 cytokines (TNF-α, IL-6) and increased the population of classically activated macrophages (M1 phenotype). These changes could be responsible, at least in part, for neuronal loss and may also induce the demyelination of axons found in CSM and OPLL; however, they could also induce alternative activation by Th2 cytokines (IL-4, -10, and -13) and increase M2 microglia/macrophages, which provide neuroprotection and enhanced phagocytic activity. This work provides the rationale for therapeutic targeting of alternative activation of microglia/macrophages in human CSM and OPLL.

Supporting Information

Figure S1 **Assessment of aging effects in control ICR mice by immunofluorescent staining.** (A) Immunofluorescence staining for the expression of CD11b (red) and NeuN (green) in 12-, 18- and 24-week-old ICR mice. (B) Immunofluorescence staining for the expression of iNOS and CD16/32 (green) identifying classically activated microglia/macrophages (M1 phenotype) and arginase-1 and CD206 (green) characterizing alternatively activated microglia/macrophages (M2 phenotype); co-localized with CD11b (red) in the anterior column of 12-, 18- and 24-week-old ICR mice. (C) Immunostaining of infiltrating helper T cells in 12-, 18- and 24-week-old ICR mice. In these

assessments, there were no differences between samples from different ages. Scale bars = 500 μm (A-upper row, C), 50 μm (A-lower row, B).
(TIF)

Figure S2 Assessment of aging effect in control ICR mice by flow cytometry and immunoblot analysis. (A) Semi-quantitative flow cytometric analysis of resting microglia and activated microglia/macrophages in the CD11b [positive] cells in 12-, 18- and 24-week-old ICR mice. (B) Immunoblot analysis of T helper 1 (Th1), T helper 2 (Th2) cytokines, neurotrophic factors and phagocytic activity in 12-, 18- and 24-week-old ICR mice. In these assessments, there were no differences between samples from different ages.
(TIFF)

Figure S3 Characterization of resting microglia population in spinal cord of twy/twy mice. Semi-quantitative analysis for iNOS, CD16/32, arginase-1, and CD206 in resting microglia was performed in flow cytometry. Representative data of 12- (A), 18- (B), and 24- (C) week-old twy/twy mice (n = 3 for each time point). Arginase-1 [positive] resting microglia constituted 10.2±2.2% (458±97 cells) and 73.0±16.1% (4017±884 cells) of the cells in 12- and 18-week-old mice. The number of arginase-1 [positive] resting microglia in control ICR mice was same as in 12-week-old twy/twy mice. Only a few iNOS-, CD16/32- and CD206-positive resting microglia were present in control ICR and twy/twy mice (D). Data are mean±SD.
(TIF)

Figure S4 Assessment of the neutrophil populations and myeloperoxidase (MPO) activity in the spinal cord of twy/twy mice. To examine the presence of neutrophils in the compressed spinal cord, we examined the presence of MPO by immunohistochemistry and by assay for MPO activity. MPO immunostaining demonstrated the lack of infiltration of neutrophils (A–C), whereas biochemical assay indicated a very small amount of MPO activity (D) irrespective of the severity of the spinal cord compression (n = 3 for each time point). Scale bars = 500 μm. Data are mean±SD.
(TIF)

Table S1 This table shows experimental groups used in the present study.
(DOCX)

Acknowledgments

Author Contributions

Conceived and designed the experiments: KU HN HB. Performed the experiments: TH ARG NT SW DS AY. Analyzed the data: TH KU HN NT. Contributed reagents/materials/analysis tools: TH HN ARG NT SW DS AY. Wrote the paper: TH KU HN ARG WEBJ HB.

References

1. Bohlman HH, Emery SE (1988) The pathophysiology of cervical spondylosis and myelopathy. Spine 13: 843–846.
2. Fehlings MG, Skaf G (1988) A review of the pathophysiology of cervical spondylotic myelopathy with insights for potential novel mechanisms drawn from traumatic spinal cord injury. Spine 23: 2730–2737.
3. Matsunaga S, Nakamura K, Seichi A, Yokoyama T, Toh S, et al. (2008) Radiographic predictors for the development of myelopathy in patients with ossification of the posterior longitudinal ligament: a multicenter cohort study. Spine 33: 2648–2650.
4. McCormack BM, Weinstein PR (1996) Cervical spondylosis. An update. West J Med 165: 43–51.
5. Kameyama T, Hashizume Y, Ando T, Takahashi A, Yanagi T, et al. (1995) Spinal cord morphology and pathology in ossification of the posterior longitudinal ligament. Brain 118: 263–278.
6. Mizuno J, Nakagawa H, Chang HS, Hashizume Y (2005) Postmortem study of the spinal cord showing snake-eyes appearance due to damage by ossification of the posterior longitudinal ligament and kyphotic deformity. Spinal Cord 43: 503–507.
7. Yu WR, Liu T, Kiehl TR, Fehlings MG (2011) Human neuropathological and animal model evidence supporting a role for Fas-mediated apoptosis and inflammation in cervical spondylotic myelopathy. Brain 134: 1277–1292.
8. Inukai T, Uchida K, Nakajima H, Yayama T, Kobayashi S, et al. (2009) Tumor necrosis factor-alpha and its receptors contribute to apoptosis of oligodendrocytes in the spinal cord of spinal hyperostotic mouse (twy/twy) sustaining chronic mechanical compression. Spine 34: 2848–2857.
9. Uchida K, Nakajima H, Watanabe S, Yayama T, Guerrero AR, et al. (2012) Apoptosis of neurons and oligodendrocytes in the spinal cord of spinal hyperostotic mouse (twy/twy): possible pathomechanism of human cervical compressive myelopathy. Eur Spine J 21: 490–497.
10. Hausmann ON (2003) Post-traumatic inflammation following spinal cord injury. Spinal Cord 41: 369–378.
11. Jones TB, McDaniel EE, Popovich PG (2005) Inflammatory-mediated injury and repair in the traumatically injured spinal cord. Curr Pharm Des 11: 1223–1236.
12. Pineau I, Sun L, Bastien D, Lacroix S (2010) Astrocytes initiate inflammation in the injured mouse spinal cord by promoting the entry of neutrophils and inflammatory monocytes in an IL-1 receptor/MyD88-dependent fashion. Brain Behav Immun 24: 540–553.
13. Popovich PG, Wei P, Stokes BT (1997) Cellular inflammatory response after spinal cord injury in Sprague-Dawley and Lewis rats. J Comp Neurol 377: 443–464.
14. Beattie MS, Hermann GE, Rogers RC, Bresnahan JC (2002) Cell death in models of spinal cord injury. Prog Brain Res 137: 37–47.
15. Crowe MJ, Bresnahan JC, Shuman SL, Masters JN, Beattie MS (1997) Apoptosis and delayed degeneration after spinal cord injury in rats and monkeys. Nat Med 3: 73–76.
16. Popovich PG, Guan Z, McGaughy V, Fisher L, Hickey WF, et al. (2002) The neuropathological and behavioral consequences of intraspinal microglial/macrophage activation. J Neuropathol Exp Neurol 61: 623–633.
17. Perego C, Fumagalli S, De Simoni MG (2011) Temporal pattern of expression and colocalization of microglia/macrophage phenotype markers following brain ischemic injury in mice. J Neuroinflammation 8: 174.
18. Glass CK, Saijo K, Winner B, Marchetto MC, Gage FH (2010) Mechanisms underlying inflammation in neurodegeneration. Cell 140: 918–934.
19. Bomstein Y, Marder JB, Vitner K, Smirnov I, Lisaey G, et al. (2003) Features of skin-coincubated macrophages that promote recovery from spinal cord injury. J Neuroimmunol 142: 10–16.
20. Stout RD, Jiang C, Matta B, Tietzel I, Watkins SK, et al. (2005) Macrophages sequentially change their functional phenotype in response to changes in microenvironmental influences. J Immunol 175: 342–349.
21. Mantovani A, Sozzani S, Locati M, Allavena P, Sica A (2002) Macrophage polarization: tumor-associated macrophages as a paradigm for polarized M2 mononuclear phagocytes. Trends Immunol 23: 549–555.
22. Kigerl KA, Gensel JC, Ankeny DP, Alexander JK, Donnelly DJ, et al. (2009) Identification of two distinct macrophage subsets with divergent effects causing either neurotoxicity or regeneration in the injured mouse spinal cord. J Neurosci 29: 13435–13444.
23. Schwartz M (2010) "Tissue-repairing" blood-derived macrophages are essential for healing of the injured spinal cord: From skin-activated macrophages to infiltrating blood-derived cells? Brain Behav Immun 24: 1054–1057.
24. Wong SC, Puaux AL, Chittezhath M, Shalova I, Kajiji TS, et al. (2010) Macrophage polarization to a unique phenotype driven by B cells. Eur J Immunol 40: 2296–2307.
25. David S, Kroner A (2011) Repertoire of microglial and macrophage responses after spinal cord injury. Nat Rev Neurosci 12: 388–399.
26. Gordon S (2003) Alternative activation of macrophages. Nat Rev Immunol 3: 23–35.
27. Laskin DL (2009) Macrophages and inflammatory mediators in chemical toxicity: a battle of forces. Chem Res Toxicol 22: 1376–1385.
28. Mantovani A, Sica A, Sozzani S, Allavena P, Vecchi A, et al. (2004) The chemokine system in diverse forms of macrophage activation and polarization. Trends Immunol 25: 677–686.
29. Gordon S, Martinez FO (2010) Alternative activation of macrophages: mechanism and functions. Immunity 32: 593–604.
30. Ma J, Chen T, Mandelin J, Ceponis A, Miller NE, et al. (2003) Regulation of macrophage activation. Cell Mol Life Sci 60: 2334–2346.

–660–

31. Busch SA, Hamilton JA, Horn KP, Cuascut FX, Cutrone R, et al. (2011) Multipotent adult progenitor cells prevent macrophage-mediated axonal dieback and promote regrowth after spinal cord injury. J Neurosci 31: 944–953.

32. Michelucci A, Heurtaux T, Grandbarbe L, Morga E, Heuschling P (2009) Characterization of the microglial phenotype under specific pro-inflammatory and anti-inflammatory conditions: Effects of oligomeric and fibrillar amyloid-beta. J Neuroimmunol 210: 3–12.

33. Baba H, Maezawa Y, Imura S, Kawahara N, Nakahashi K, et al. (1996) Quantitative analysis of the spinal cord motoneuron under chronic compression: an experimental observation in the mouse. J Neurol 243: 109–116.

34. Okawa A, Nakamura I, Goto S, Moriya H, Nakamura Y, et al. (1998) Mutation in Npps in a mouse model of ossification of the posterior longitudinal ligament of the spine. Nat Genet 19: 271–273.

35. Uchida K, Baba H, Maezawa Y, Furukawa S, Furusawa N, et al. (1998) Histological investigation of spinal cord lesions in the spinal hyperostotic mouse (twy/twy): morphological changes in anterior horn cells and immunoreactivity to neurotrophic factors. J Neurol 245: 781–793.

36. Uchida K, Baba H, Maezawa Y, Furukawa S, Omiya M, et al. (2003) Increased expression of neurotrophins and their receptors in the mechanically compressed spinal cord of the spinal hyperostotic mouse (twy/twy). Acta Neuropathol 106: 29–36.

37. Yu WR, Baptiste DC, Liu T, Odrobina E, Stanisz GJ, et al. (2009) Molecular mechanisms of spinal cord dysfunction and cell death in the spinal hyperostotic mouse: implications for the pathophysiology of human cervical spondylotic myelopathy. Neurobiol Dis 33: 149–163.

38. Saiwai H, Ohkawa Y, Yamada H, Kumamaru H, Harada A, et al. (2010) The LTB4-BLT1 axis mediates neutrophil infiltration and secondary injury in experimental spinal cord injury. Am J Pathol 176: 2352–2366.

39. Stirling DP, Yong VW (2008) Dynamics of the inflammatory response after murine spinal cord injury revealed by flow cytometry. J Neurosci Res 86: 1944–1958.

40. Schilling M, Besselmann M, Muller M, Strecker JK, Ringelstein EB, et al. (2005) Predominant phagocytic activity of resident microglia over hematogenous macrophages following transient focal cerebral ischemia: an investigation using green fluorescent protein transgenic bone marrow chimeric mice. Exp Neurol 196: 290–297.

41. Shuman SL, Bresnahan JC, Beattie MS (1997) Apoptosis of microglia and oligodendrocytes after spinal cord contusion in rats. J Neurosci Res 50: 798–808.

42. Mukaino M, Nakamura M, Yamada O, Okada S, Morikawa S, et al. (2010) Anti-IL-6-receptor antibody promotes repair of spinal cord injury by inducing microglia-dominant inflammation. Exp Neurol 224: 403–414.

43. Pineau I, Lacroix S (2007) Proinflammatory cytokine synthesis in the injured mouse spinal cord: multiphasic expression pattern and identification of the cell types involved. J Comp Neurol 500: 267–285.

44. Ethuin F, Gerard B, Benna JE, Boutten A, Gougereot-Pocidalo MA, et al. (2004) Human neutrophils produce interferon gamma upon stimulation by interleukin-12. Lab Invest 84: 1363–1371.

45. Suzuki Y, Claflin J, Wang X, Lengi A, Kikuchi T (2005) Microglia and macrophages as innate producers of interferon-gamma in the brain following infection with Toxoplasma gondii. Int J Parasitol 35: 83–90.

46. Ponomarev ED, Maresz K, Tan Y, Dittel BN (2007) CNS-derived interleukin-4 is essential for the regulation of autoimmune inflammation and induces a state of alternative activation in microglial cells. J Neurosci 27: 10714–10721.

47. Shin WH, Lee DY, Park KW, Kim SU, Yang MS, et al. (2004) Microglia expressing interleukin-13 undergo cell death and contribute to neuronal survival in vivo. Glia 46: 142–152.

48. Guerrero AR, Uchida K, Nakajima H, Watanabe S, Nakamura M, et al. (2012) Blockade of interleukin-6 signaling inhibits the classic pathway of macrophage activation after spinal cord injury in mice. J Neuroinflammation 9: 40.

—661—

^{18}F-FDG PET/CT for Diagnosis of Osteosclerotic and Osteolytic Vertebral Metastatic Lesions: Comparison with Bone Scintigraphy

Kenzo Uchida[1], Hideaki Nakajima[1], Tsuyoshi Miyazaki[1], Tatsuro Tsuchida[2],
Takayuki Hirai[1], Daisuke Sugita[1], Shuji Watanabe[1], Naoto Takeura[1],
Ai Yoshida[1], Hidehiko Okazawa[3], Hisatoshi Baba[1]

[1]Departments of Orthopaedics and Rehabilitation Medicine, University of Fukui, Fukui, Japan
[2]Departments of Radiology, Faculty of Medical Sciences, University of Fukui, Fukui, Japan
[3]Biomedical Imaging Research Center, University of Fukui, Fukui, Japan

Study Design: A retrospective study.

Purpose: The aims of this study were to investigate the diagnostic value of ^{18}F-fluorodeoxyglucose (FDG) positron emission tomography (PET) in PET/computed tomography (CT) in the evaluation of spinal metastatic lesions.

Overview of Literature: Recent studies described limitations regarding how many lesions with abnormal ^{18}F-FDG PET findings in the bone show corresponding morphologic abnormalities.

Methods: The subjects for this retrospective study were 227 patients with primary malignant tumors, who were suspected of having spinal metastases. They underwent combined whole-body ^{18}F-FDG PET/CT scanning for evaluation of known neoplasms in the whole spine. ^{99m}Tc-methylene diphosphonate bone scan was performed within 2 weeks following PET/CT examinations. The final diagnosis of spinal metastasis was established by histopathological examination regarding bone biopsy or magnetic resonance imaging (MRI) findings, and follow-up MRI, CT and ^{18}F-FDG PET for extensively wide lesions with subsequent progression.

Results: From a total of 504 spinal lesions in 227 patients, 224 lesions showed discordant image findings. For 122 metastatic lesions with confirmed diagnosis, the sensitivity/specificity of bone scan and FDG PET were 84%/21% and 89%/76%, respectively. In 102 true-positive metastatic lesions, the bone scan depicted predominantly osteosclerotic changes in 36% and osteolytic changes in 19%. In 109 true-positive lesions of FDG PET, osteolytic changes were depicted predominantly in 38% while osteosclerotic changes were portrayed in 15%.

Conclusions: ^{18}F-FDG PET in PET/CT could be used as a substitute for bone scan in the evaluation of spinal metastasis, especially for patients with spinal osteolytic lesions on CT.

Keywords: ^{18}F-fluorodeoxyglucose positron emission tomography; Technetium Tc 99m (Sn)methylenediphosphonate; Positron emission tomography and computed tomography; Spine; Metastasis

Introduction

Very few factors can change the strategy for cancer treatment, including spine surgery, in such a radical way as the presence or absence of bone metastases assessed during the initial stage or during follow up. The vertebral column is the region of the skeleton most frequently affected by metastasis. The tumors that most commonly metastasize to the vertebrae are carcinomas of the breast in women and carcinomas of the lung and prostate in men; however, metastases are also frequently seen in patients with lymphoma and multiple myeloma [1,2]. It is well known that vertebral metastases represent hematogenous dissemination of the primary tumor, direct extension through the intervertebral foramina or invasion of the epidural space from adjacent vertebral segments. Metastatic lesions often cause compression of the adjacent neural structures such as the spinal cord, cauda equine and/or nerve roots and in the latter, they are often associated with radiculopathy [1]. In order to increase the chances of a favorable outcome, the most important issue remains avoiding the development of any permanent neurological or functional deficit through early diagnosis and treatment [3]. While in a selected group of patients a combined approach; including chemotherapy and surgery; may be plausible for the treatment of metastatic spinal tumors, radiation remains the primary choice [4].

The most commonly used imaging procedure for the assessment of bone metastases is ^{99m}Tc-methylene diphosphonate (MDP) bone scintigraphy, though it cannot detect accompanying soft-tissue abnormalities and lacks specificity, given the multiplicity of abnormal, but benign processes, that could affect bones, leading to false negative and positive results [5]. On the other hand, ^{18}F-fluorodeoxyglucose (FDG) positron emission tomography (PET) is more sensitive than bone scintigraphy in patients with lung cancer and lymphoma, and can detect early bone marrow involvement including spinal metastasis before the appearance of cortical changes on bone scintigraphy [6,7]. With the increased use of whole-body ^{18}F-FDG PET for the staging and follow-up of malignant diseases, it is not uncommon to encounter vertebral metastases. Recent studies described limitations regarding how many lesions with abnormal ^{18}F-FDG PET findings in bone show corresponding morphologic abnormalities, even if they are not suspected of representing definite bone metastasis [8]. Other studies have reported false-positive [18]F-

FDG PET results in patients suspected of bone metastases [9]. Due to these limitations, several clinical applications have become available for use with the recently released generation of combined PET/computed tomography (CT) scanners [10-12]; which can provide detailed anatomic information and abnormal findings beyond the capabilities of the PET scanner alone [13]. At present, detection of bone metastases on the PET is usually followed by the CT for assessment of the morphologic features regarding the lesions [14].

The present study was designed to retrospectively investigate the diagnostic values of ^{18}F-FDG PET in the evaluation of spinal metastases and to compare ^{18}F-FDG PET in PET/CT with the conventional ^{99m}Tc-MDP bone scan, and to assess the added value of CT in PET/CT studies in lesion detection and localization of vertebral lesions, and to correlate between the morphological changes detected on CT and the positive findings of ^{18}F-FDG PET findings or bone scan in spinal metastatic lesions.

Materials and Methods

1. Study cohort

The subjects of this retrospective study were 227 patients (121 men, 106 women; age range, 35–82 years; mean, 59.9) with primary malignant tumors in the lung (n=91), breast (n=43), gastrointestinal tract (n=33) (esophageal, gastric and colonic cancers), kidney (n=21), prostate (n=15), uterus or ovaries (n=10), lymph nodes (n=8, malignant lymphoma), head and neck (n=3), and bone and soft tissues (n=3), who were suspected of having spinal metastases. They underwent combined whole-body PET/CT scanning for evaluation of known neoplasms in the whole spine between January 2005 and December 2008. ^{99m}Tc-MDP bone scan was performed within 2 weeks after PET/CT examinations. The final diagnosis of spinal metastasis was established by a histopathological examination of the bone biopsy or MRI findings, and a follow-up MRI, CT, and ^{18}F-FDG PET of extensively wide lesions with subsequent progression.

2. ^{99m}Tc-MDP bone scans

Routine bone scans were obtained with a large field-of-view, dual-head gamma camera (E-CAM, Siemens Medical System, Hoffman Estates, IL, USA) with a low-energy

Table 1. Differences between morphological changes on CT with true-positive lesions on each bone scan or FDG PET

	Bone scan (n=102)	FDG PET (n=109)	p-value	SUV	
				Mean	Range
None	32 (31.4)	35 (32.1)	NS	-	-
Non-specific	14 (13.7)	17 (15.6)	NS	-	-
Osteolytic changes	19 (18.6)	41 (37.6)	<0.05	8.67	5.6-15.7
Osteosclerotic changes	37 (36.3)	16 (14.7)	<0.05	1.27	0.1-2.6

Values are presented as bone scan and FDG PET represent number of lesions.
Data in parentheses are percentages.
$p < 0.05$; for "Bone scan" and "FDG PET" (by Mann-Whitney U-test).
CT, computed tomography; FDG, fluorodeoxyglucose; PET, positron emission tomography; SUV, standardized uptake value; NS, not significant.

high-resolution collimator. Anterior and posterior whole-body images were acquired 3 hours after an intravenous injection of approximately 740 MBq of ^{99m}Tc-MDP.

3. PET/CT scanning

^{18}F-FDG PET/CT was performed using a combined PET/CT scanner (Discovery LS, General Electric Medical Systems, Waukesha, WI, USA). For the PET/CT scanners, 35 transaxial images were acquired simultaneously per field of view with an interslice spacing of 4.25 mm. The PET/CT scanner incorporates an integrated 4-slice multidetector CT scanner, which was used for attenuation correction. The CT scanning parameters were as follows: Auto mA (upper limit, 40 mA; noise index, 20), 140 kV, 5-mm section thickness, 15-mm table feed, and pitch of 4. After at least 4 hours of fasting, the patient received an intravenous injection of 185 MBq of ^{18}F-FDG and image acquisition began 50 minutes after injection. A whole-body emission scan was performed from the head to the inguinal region with 2 minutes per bed position (7–8 bed positions). A transmission scan with CT was performed prior to the emission scan. CT images for attenuation correction were applied to the emission data and the attenuation-corrected emission images were reconstructed with an ordered-subset expectation maximization iterative reconstruction algorithm (2 iterations, 14 subsets).

4. Image analysis

Two experienced physicians (H.N., T.H.) identified the spinal lesions on bone scans as sites of increased MDP uptake relative to the surrounding normal bone activity.

Whole-body FDG PET skeletal images were independently and visually analyzed by two experienced physicians (T.M., T.T.) on a high-resolution display to compare them with the corresponding ^{99m}Tc-MDP whole-body bone scan findings. A spinal lesion on ^{18}F-FDG PET was defined as a focus of increased ^{18}F-FDG uptake, above the intensity of the surrounding normal bone activity, excluding the physiologically increased ^{18}F-FDG uptake areas of renal pelvis, urinary bladder, bowel, myocardium, and brain. In order to examine the differences between morphological changes on the CT with the true-positive lesions at each bone scan or FDG PET, a region of interest (ROI; size, 20×20 mm) was placed by one author (T.M.) over all suspected lesions, and the maximal single pixel value was determined for each lesion on the whole spine. The standardized uptake value (SUV) was calculated using the following formula: $SUV=ROI_{RC}/(ID/BW)$; where ROI_{RC} is the radioactivity concentration within the region of interest (in becquerels per milliliter), ID is the injected dose of ^{18}F-FDG (in becquerels), and BW is body weight in grams.

The CT images were evaluated by two physicians (D.S., S.W.) using CT planes that corresponded to the planes in which the lesion appeared on the FDG PET. The physicians were aware of the positive spinal lesions on the PET, and they used a workstation to display the CT scans with the bone and soft-tissue windows. The CT analysis determined the presence or absence of spinal metastasis and the type of morphologic changes (nonspecific, osteolytic, osteosclerotic). Nonspecific changes represented abnormal CT findings that were neither neoplastic nor degenerative changes [14]. Lesions exhibiting both osteolytic and osteosclerotic changes were considered to be either

type based on the predominant change in that lesion.

5. Statistical analysis

The Mann-Whitney U-test was used to compare differences between the percentages of patients being evaluated through "Bone scan" and "FDG PET" (Table 1). A probability value less than 0.05 denoted statistical significance. All statistical analyses were conducted using SPSS software (ver. 15.0, SPSS, Chicago, IL, USA).

Results

A total of 504 spinal lesions in 227 patients found on either bone scans or FDG PETs were evaluated. Positive FDG PET as well as positive bone scan findings were identified in 280 spinal lesions. In the remaining 224 lesions with discordant findings, 68 had positive bone scan images, but negative FDG PETs, while 156 had negative bone scans but positive FDG PETs (Table 2). In 156 spinal lesions (cervical 25, thoracic 90, and lumbar 41), including 22 examined histopathologically, the final diagnosis
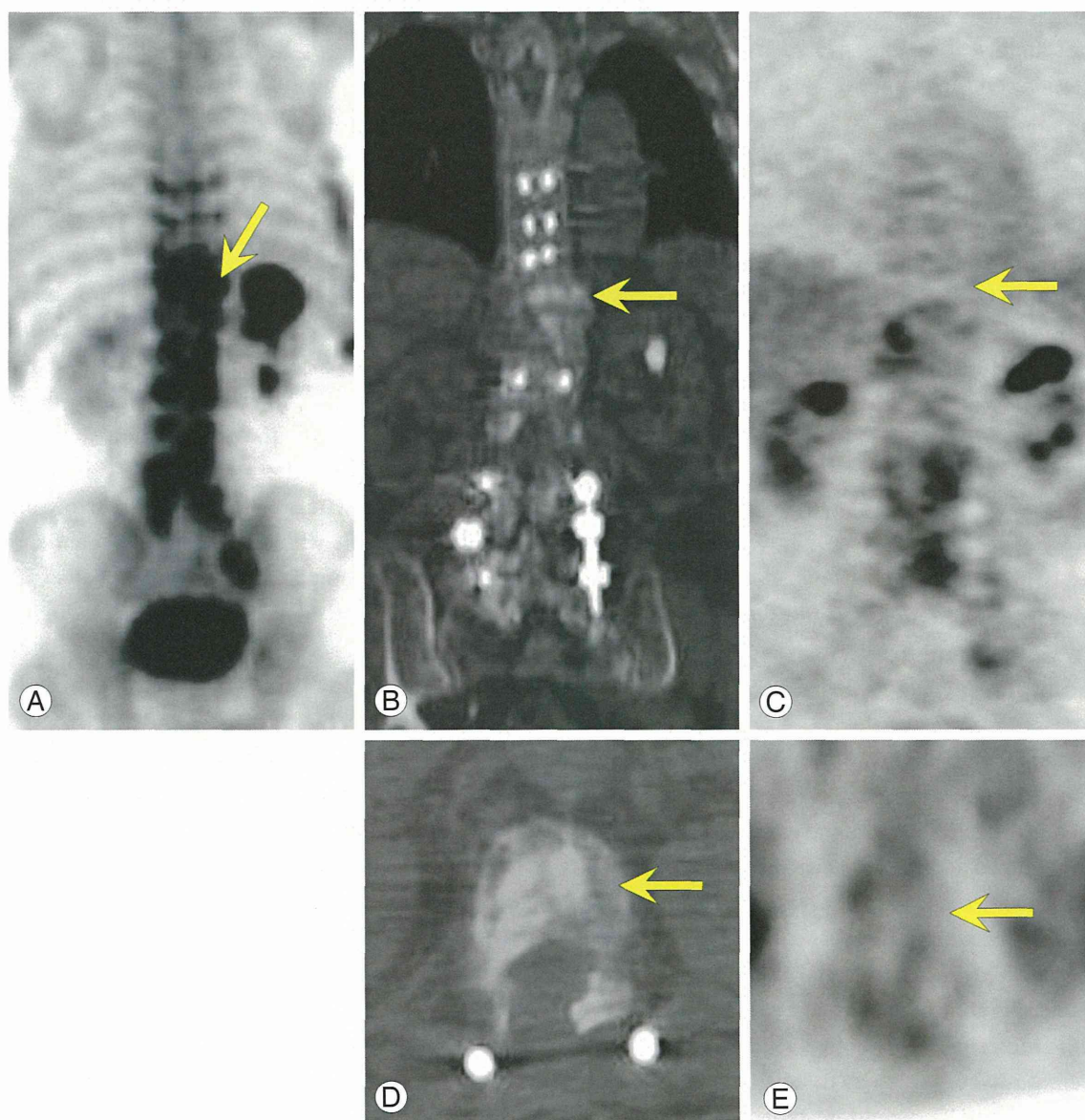
Fig. 1. Bone scan **(A)**, CT, **(B, D)** and FDG PET **(C, E)** images of a 77-year-old man with prostate carcinoma. Note the focal intense uptake of osteoblastic spine metastases (vertebral body of T11) on the bone scan only but not on the PET images (arrows). Axial and coronal CT images show ostesclerotic changes in the vertebral body **(B, D)** and no focal intense uptake on the PET images **(C, E)**. CT, computed tomography; FDG, fluorodeoxyglucose; PET, positron emission tomography.

was 122 spinal metastatic lesions and 34 benign lesions. Of the 122 metastatic lesions, positive bone scan findings were recorded in 102 lesions and negative findings were recorded in 20 lesions. Positive FDG PET findings were recorded in 109 lesions and negative findings were recorded in 13 lesions. The sensitivity with regards to bone scans and FDG PETs were 84% and 89%, respectively. In contrast, for the 34 benign lesions, the positive and negative bone scan findings were recorded in 27 and 7 lesions, respectively, whereas positive and negative FDG PET findings were recorded in 8 and 26 lesions, respectively (the specificity for bone scans and FDG PETs were 21% and 76%, respectively) (Table 3).

The morphological changes were determined for true-positive lesions on each bone scan (102 lesions) and FDG PET (109 lesions) (Table 1). No changes on CT were seen for bone scans in 32 lesions (31%), and on FDG PETs in 35 lesions (32%). Bone scans depicted predominantly sclerotic changes in 37 lesions (36%) and mainly osteolytic changes in 19 lesions (19%) (Fig. 1). On the other hand, FDG PETs depicted predominantly osteolytic changes in 41 lesions (38%) and mainly osteosclerotic changes in 16 lesions (15%) (Fig. 2).

Discussion

In the assessment of spine tumors, while evaluating the epidural extension or marrow involvement, the MRI remains as the gold standard [15-18]. However, when evaluating large numbers of screenings in suspected bone metastases cases, bone scintigraphy is the most common modality used due to its high sensitivity, availability, cost, and ease of surveying the entire skeleton. However, many patients with bone metastases do not show typical or specific patterns on these scans [5,19]. Several factors can influence the tracer uptake, such as degenerative joint disease and related benign bone diseases or osteocartilaginous abnormalities, such as previous skeletal trauma; all of which will finally limit the specificity of the bone scan. Since the conventional bone scan is sensitive enough to detect accelerated osteoblastic activities, which are nonspecific indicators of pathology; the image provided by a different modality such as tissue glucose utilization mapped with ^{18}F-FDG, would be expected to provide a different view of bone pathology. Tumor cells release a myriad of biologically active substances that could actively interfere with glycolysis, following tumor invasion.

Table 2. Distribution of bone scan and FDG PET findings in spinal lesions examined in present study

Bone scan	FDG PET	
	Positive	Negative
Positive	280	68
Negative	156	Undefined

Values are presented as number of lesions.
FDG, fluorodeoxyglucose; PET, positron emission tomography.

Table 3. Distribution of bone scan/FDG PET findings based on final diagnosis in all spinal lesions

	Bone metastatic (Bone scan/FDG PET)	Benign (Bone scan/FDG PET)
Positive	102/109	27/8
Negative	20/13	7/26

Values are presented as number of lesions.
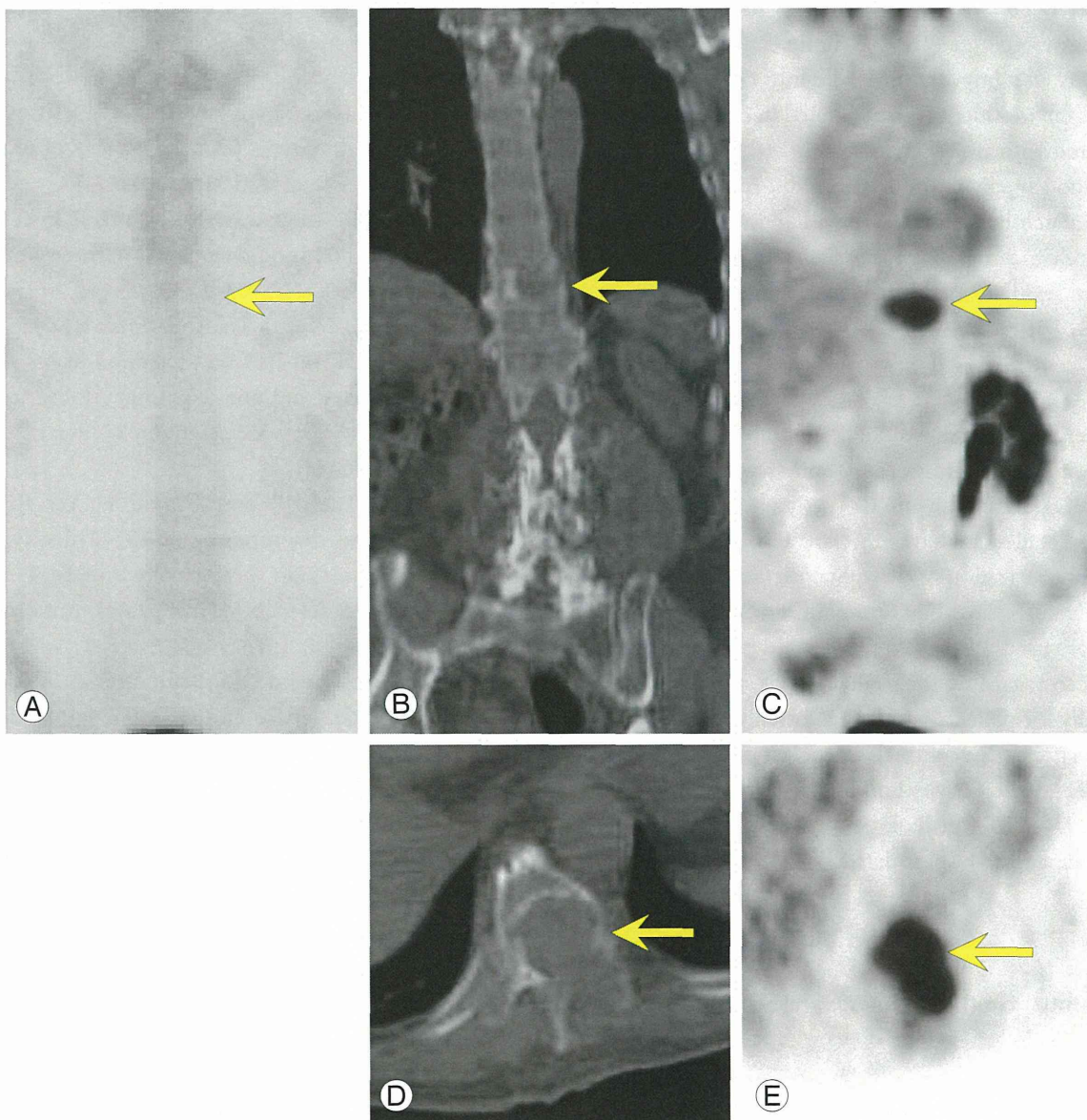FDG, fluorodeoxyglucose; PET, positron emission tomography.

Therefore, not only the measurement of mineral turnover, as conventionally achieved in bone scans, but also the assessment of glucose metabolic processes, could be of great significance for differentiating benign from malignant bone lesions [20]. The present study was undertaken in order to evaluate the usefulness of ^{18}F-FDG PET in measuring glycolytic activity in bone marrow metastatic lesions in patients with suspected malignant spinal metastases, and to compare bone scans and FDG PETs in the detection of spinal metastases. Our results indicate that ^{18}F-FDG PET is potentially useful for the detection of vertebral metastatic lesions based on the analysis of 122 spinal lesions.

Several studies compared bone scans to FDG PETs in the detection of different types of cancers [21,22]. FDG PETs were superior to bone scans in the detection of breast cancer in patients with known skeletal metastases; with the exception of a subgroup of patients with osteoblastic metastases [23], though the bone scan had been reported to be superior than PET in detecting osteoblastic metastatic lesions [22]. Such data emphasize the complementary nature of bone scans and FDG PETs in the evaluation of skeletal metastases in breast cancer patients, as reported previously [24]; as well as in the staging of bone metastasis in breast cancer, where each modality cannot substitute the other. It has been reported already that the FDG PET is less sensitive than the bone scan in

prostate cancers [25]; where the FDG with a sensitivity of 65%, only identified 131 of 202 untreated metastases in a group of 22 patients [26]. Morris et al. [27] found that the bone scan was significantly more sensitive (94%) than the FDG (77%) in a series of 134 bone metastases. While the FDG appears to be quite useful in the detection of bone metastases from lung cancer, it is not so effective in prostate cancers due to the osteoblastic characteristics of the lesions [25]. A higher accuracy of PET in the detection of bone metastases, relative to the bone scan, was also reported [7]. Thus, it is clear that PETs and bone scans provide different diagnoses according to the type of the primary cancer, being an important limitation to our study, and implies the need for larger studies to examine each primary cancer.

In our research, among the lesions finally diagnosed as metastases using all the available resources; the CT characterized only 31% to 32% as probable or definite metastases whereas the remaining 68% to 69% of the lesions was undiagnosed. Furthermore, while morphologic changes were often identified using bone windows to display the CT images, only 50% of the lesions depicted

Fig. 2. Bone scan (A), computed tomography (CT) (B, D) and fluorodeoxyglucose (FDG) positron emission tomography (PET) (C, E) images of a 69-year-old man with renal cell carcinoma. Note the focal intense uptake in osteolytic spine metastases (vertebral body of T10) on PET only but not on the bone scan (arrows). Axial and coronal CT images show osteolytic changes in the vertebral body (B, D) and focal intense uptake on the PET images (C, E).

minimal and more marked osteolytic or osteoblastic changes. These findings emphasize the limitations of the CT in confirming or excluding bone metastases detected on bone scans or PETs.

Our results also demonstrated differences in the detection of osteolytic versus osteoblastic lesions; where FDG-PET showed a higher sensitivity in the detection of osteolytic lesions, but lower sensitivity, relative to bone scans, in osteoblastic metastases. Whether the greater avidity for ^{18}F-FDG in osteolytic metastases reflects a higher glycolytic rate in this type of lesion remains unknown; and since osteoblastic metastases are relatively acellular [28], the degree of ^{18}F-FDG uptake may be influenced by the lower volume of viable tumor tissue within the lesion. It is also important to take into consideration the hypoxic environment typically noted in osteolytic lesions, compared with osteoblastic lesions, which is caused by poor blood supply in these lesions due to their aggressive growth. Such behavior may be an additional factor that could influence the diagnosis, since hypoxia is known to increase ^{18}F-FDG uptake in some cell lines [29].

Conclusions

The present study showed a comparable diagnostic accuracy of spinal metastases by bone scan and FDG PET in PET/CT. Although the CT (as part of PET/CT) can provide detailed anatomic information, our data suggest that characterization of the spinal metastatic lesions is of limited value even when optimal CT window width and level were used. PET in PET/CT could be a substitute for bone scan regarding the evaluation of spinal metastasis, especially for patients with spinal osteolytic lesions identified on the CT. In contrast, osteoblastic metastases show lower metabolic activity and are frequently undetectable on the FDG PET. The biologic explanation for this observation remains to be elucidated.

Conflict of Interest

No potential conflict of interest relevant to this article was reported.

References

1. Rodriguez M, Dinapoli RP. Spinal cord compression: with special reference to metastatic epidural tumors. Mayo Clin Proc 1980;55:442-8.
2. Schiff D, O'Neill BP, Suman VJ. Spinal epidural metastasis as the initial manifestation of malignancy: clinical features and diagnostic approach. Neurology 1997;49:452-6.
3. Bilsky MH, Lis E, Raizer J, Lee H, Boland P. The diagnosis and treatment of metastatic spinal tumor. Oncologist 1999;4:459-69.
4. Tomita K, Kawahara N, Kobayashi T, Yoshida A, Murakami H, Akamaru T. Surgical strategy for spinal metastases. Spine (Phila Pa 1976) 2001;26:298-306.
5. Jocobson AF. Bone scanning in metastatic disease. In: Collier DC, Fogelman I, Rosenthall L, editors. Skeletal nuclear medicine. St. Louis, MO: Mosby; 1996. p.87-123.
6. Moog F, Kotzerke J, Reske SN. FDG PET can replace bone scintigraphy in primary staging of malignant lymphoma. J Nucl Med 1999;40:1407-13.
7. Marom EM, McAdams HP, Erasmus JJ, et al. Staging non-small cell lung cancer with whole-body PET. Radiology 1999;212:803-9.
8. Franzius C, Sciuk J, Daldrup-Link HE, Jurgens H, Schober O. FDG-PET for detection of osseous metastases from malignant primary bone tumours: comparison with bone scintigraphy. Eur J Nucl Med 2000;27:1305-11.
9. Kao CH, Hsieh JF, Tsai SC, Ho YJ, Yen RF. Comparison and discrepancy of 18F-2-deoxyglucose positron emission tomography and Tc-99m MDP bone scan to detect bone metastases. Anticancer Res 2000;20:2189-92.
10. Beyer T, Townsend DW, Brun T, et al. A combined PET/CT scanner for clinical oncology. J Nucl Med 2000;41:1369-79.
11. Kluetz PG, Meltzer CC, Villemagne VL, et al. Combined PET/CT imaging in oncology. Impact on patient management. Clin Positron Imaging 2000;3:223-30.
12. Kaim AH, Burger C, Ganter CC, et al. PET-CT-guided percutaneous puncture of an infected cyst in autosomal dominant polycystic kidney disease: case report. Radiology 2001;221:818-21.
13. Metser U, Lerman H, Blank A, Lievshitz G, Bokstein F, Even-Sapir E. Malignant involvement of the spine: assessment by 18F-FDG PET/CT. J Nucl Med 2004;45:279-84.
14. Nakamoto Y, Cohade C, Tatsumi M, Hammoud D,

Wahl RL. CT appearance of bone metastases detected with FDG PET as part of the same PET/CT examination. Radiology 2005;237:627-34.

15. Kim JK, Learch TJ, Colletti PM, Lee JW, Tran SD, Terk MR. Diagnosis of vertebral metastasis, epidural metastasis, and malignant spinal cord compression: are T(1)-weighted sagittal images sufficient? Magn Reson Imaging 2000;18:819-24.

16. Kim HJ, Ryu KN, Choi WS, Choi BK, Choi JM, Yoon Y. Spinal involvement of hematopoietic malignancies and metastasis: differentiation using MR imaging. Clin Imaging 1999;23:125-33.

17. Mehta RC, Marks MP, Hinks RS, Glover GH, Enzmann DR. MR evaluation of vertebral metastases: T1-weighted, short-inversion-time inversion recovery, fast spin-echo, and inversion-recovery fast spin-echo sequences. AJNR Am J Neuroradiol 1995;16:281-8.

18. Yuh WT, Zachar CK, Barloon TJ, Sato Y, Sickels WJ, Hawes DR. Vertebral compression fractures: distinction between benign and malignant causes with MR imaging. Radiology 1989;172:215-8.

19. Resnick D. Skeletal metastasis. In: Resnick D, editor. Bone and joint imaging. Philadelphia, PA: W.B. Saunders Company; 1996. p.1076-91.

20. Hawkins RA, Hoh CK. PET bone imaging. In: Collier D, Fogelman I, Rosenthall L, editors. Skeletal nuclear medicine. St. Louis, MO: Mosby; 1996. p.435-42.

21. Cheran SK, Herndon JE 2nd, Patz EF Jr. Comparison of whole-body FDG-PET to bone scan for detection of bone metastases in patients with a new diagnosis of lung cancer. Lung Cancer 2004;44:317-25.

22. Abe K, Sasaki M, Kuwabara Y, et al. Comparison of 18FDG-PET with 99mTc-HMDP scintigraphy for the detection of bone metastases in patients with breast cancer. Ann Nucl Med 2005;19:573-9.

23. Cook GJ, Houston S, Rubens R, Maisey MN, Fogelman I. Detection of bone metastases in breast cancer by 18FDG PET: differing metabolic activity in osteoblastic and osteolytic lesions. J Clin Oncol 1998;16:3375-9.

24. Eubank WB, Mankoff DA. Evolving role of positron emission tomography in breast cancer imaging. Semin Nucl Med 2005;35:84-99.

25. Fogelman I, Cook G, Israel O, Van der Wall H. Positron emission tomography and bone metastases. Semin Nucl Med 2005;35:135-42.

26. Shreve PD, Grossman HB, Gross MD, Wahl RL. Metastatic prostate cancer: initial findings of PET with 2-deoxy-2-[F-18]fluoro-D-glucose. Radiology 1996;199:751-6.

27. Morris MJ, Akhurst T, Osman I, et al. Fluorinated deoxyglucose positron emission tomography imaging in progressive metastatic prostate cancer. Urology 2002;59:913-8.

28. Galasko CS. Skeletal metastases. London: Butterwoths; 1986.

29. Clavo AC, Brown RS, Wahl RL. Fluorodeoxyglucose uptake in human cancer cell lines is increased by hypoxia. J Nucl Med 1995;36:1625-32.

BASIC SCIENCE

Indian Hedgehog Signaling Promotes Chondrocyte Differentiation in Enchondral Ossification in Human Cervical Ossification of the Posterior Longitudinal Ligament

Daisuke Sugita, MD, Takafumi Yayama, MD, DMSc, Kenzo Uchida, MD, DMSc, Yasuo Kokubo, MD, DMSc, Hideaki Nakajima, MD, DMSc, Atsushi Yamagishi, MD, Naoto Takeura, MD, and Hisatoshi Baba, MD, DMSc

Study Design. Histological, immunohistochemical, and immunoblot analyses of the expression of Indian hedgehog (Ihh) signaling in human cervical ossification of the posterior longitudinal ligament (OPLL).

Objective. To examine the hypothesis that Ihh signaling in correlation with Sox9 and parathyroid-related peptide hormone (PTHrP) facilitates chondrocyte differentiation in enchondral ossification process in human cervical OPLL.

Summary of Background Data. In enchondral ossification, certain transcriptional factors regulate cell differentiation. OPLL is characterized by overexpression of these factors and disturbance of the normal cell differentiation process. Ihh signaling is essential for enchondral ossification, especially in chondrocyte hypertrophy.

Methods. Samples of ossified ligaments were harvested from 45 patients who underwent anterior cervical decompressive surgery for symptomatic OPLL, and 6 control samples from patients with cervical spondylotic myelopathy/radiculopathy without OPLL. The harvested sections were stained with hematoxylin-eosin and toluidine blue, examined by transmission electron microscopy, and immunohistochemically stained for Ihh, PTHrP, Sox9, type X, XI collagen, and alkaline phosphatase. Immunoblot analysis was performed in cultured cells derived from the posterior longitudinal ligaments in the vicinity of the ossified plaque and examined for the expression of these factors.

Results. The ossification front in OPLL contained chondrocytes at various differentiation stages, including proliferating chondrocytes in fibrocartilaginous area, hypertrophic chondrocytes around the calcification front, and apoptotic chondrocytes near the ossified area. Immunoreactivity for Ihh and Sox9 was evident in proliferating chondrocytes and was strongly positive for PTHrP in hypertrophic chondrocytes. Mesenchymal cells with blood vessel formation were positive for Ihh, PTHrP, and Sox9. Cultured cells from OPLL tissues expressed significantly higher levels of Ihh, PTHrP, and Sox9 than those in non-OPLL cells.

Conclusion. Our results indicated that overexpression of Ihh signaling promotes abnormal chondrocyte differentiation in enchondral ossification and enhances bone formation in OPLL.

Key words: ossification of the posterior longitudinal ligament, Indian hedgehog signaling, parathyroid-related peptide hormone, enchondral ossification, chondrocyte differentiation.

Spine 2013;38:E1388–E1396

The posterior longitudinal ligament (PLL) is a 2-layer structure. The superficial layer is located in close contact with the dura mater and bridges 3 or 4 vertebrae. The deep layer is located posterior to the vertebral body and connects 2 adjacent vertebrae.[1,2] The failure of this ligament results in compression of the spinal cord with potential serious myelopathy. Ossification of the PLL (OPLL) is characterized by pathological bone formation and has been extensively investigated from various aspects.[3–5] Because this pathological entity is common in northeast Asians, recent genetic analysis suggests the involvement of certain genes, such as *COL6A1*, *COL11A2*, and/or *NPPS*.[6–8] In fact, the newest genomewide association study suggested the involvement of chromosome 6 in OPLL.[9]

Progression of OPLL is similar in style to enchondral ossification, which is usually seen at the growth plate.[10,11]

We described previously the presence of chondrocytes at the ossification front and demonstrated differences in cell aggregation and density according to the subtype of OPLL.[12–14] Furthermore, the process of enchondral ossification was regulated by various growth factors and/or transcriptional factors, although abnormal expression of these factors might be involved in the progression of OPLL.[13–18] Recent reports[19–21] have indicated the involvement of Indian hedgehog (Ihh) signaling in cell differentiation seen in enchondral ossification at normal growth plate. Thus, Ihh affects the proliferation and hypertrophy of chondrocytes through interaction with parathyroid-related peptide hormone (PTHrP).[19] However, the exact role of Ihh signaling in the pathogenesis of OPLL remains unclear.[19,20]

This study is an extension to our previous studies in human OPLL[13,16] and is designed to investigate the pathological role of Ihh signaling in chondrocyte differentiation at the ossification front, using immunohistochemical examination and biological analysis of cultured cells from surgically obtained OPLL tissue.

MATERIALS AND METHODS

Patients and Biological Samples
A total of 181 patients who presented progressive symptoms of myelopathy and/or radiculopathy and radiological evidence of OPLL (136 males and 45 females; mean age at surgery, 67.5 yr; range, 41–85 yr) underwent anterior decompressive surgery at our University Hospital between 1991 and 2012. We were able to obtain random *en bloc* samples of the ligament-ossified plaque complex from 45 patients. For cell cultures, the PLL specimens were harvested from 11 of 45 patients (8 men, 3 women; mean age 69.2 years). We also examined samples obtained from 6 age-matched control patients (OPLL-free group, 3 males, 3 females; mean age, 70.1 yr) who underwent anterior decompressive surgery.

OPLL was diagnosed by the presence of bone formation in the PLL on radiographs and/or computed tomographic scans of the cervical spine. None of the patients had evidence of congenital bone or joint disorders or musculoligamentous tissue abnormalities. None had seronegative spondyloarthropathy or hyperparathyroidism or was being treated with glucocorticoids or immunosuppressants. Surgical procedures of anterior decompression and interbody fusion were described in detail in our previous publication,[13] and all surgical procedures were performed by 2 senior authors (H.B. and K.U.). Briefly, the left-sided anterolateral approach was used to expose the affected vertebral levels. The OPLL plaque was isolated circumferentially, together with surrounding non-ossified PLL (deep layer), like a floating island on the dura mater (Figure 1A; see Supplemental Digital Content Data 1, available at http://links.lww.com/BRS/A799). Using a custom-made micro-Kerrison rongeur, we dissected carefully the non-ossified area of the ligament peripheral to the ossified lesion and removed *en bloc* with the surrounding tissues (Figure 1B; see Supplemental Digital Content Data 1, available at http://links.lww.com/BRS/A799).

A written informed consent was obtained from each patient, and the study protocol was approved by the Human Ethics Review Committee of our University Medical Faculty and strictly followed the Clinical Research Guidelines of the Ministry of Health, Labor, and Welfare of the Japanese Government.

Histological and Immunohistochemical Staining
The tissue blocks were stained immunohistochemically using the methods described previously.[13,14,16] The primary antibodies used in this study were rabbit polyclonal anti-Sox9 (lot DO406; Santa Cruz Biotechnology, Dallas, TX), rabbit polyclonal anti-Ihh (lot 20450; GeneTex, San Antonio, TX), mouse monoclonal anti-PTHrP (batch 17011; AbD Serotec, Oxford, England), mouse monoclonal anti–type X collagen (lot 350521; Quartett, Berlin, Germany), rabbit polyclonal anti-type XI collagen (lot 584061; CosmoBio, Tokyo, Japan), and rabbit monoclonal anti–bone alkaline phosphatase (lot GR79855-4; Abcamn, Cambridge, England). Signals were detected using goat anti–mouse immunoglobulin (IgG) antibodies conjugated to peroxidase-labeled dextran polymer (EnVision, peroxidase; Dako, Glostrup, Denmark) for monoclonal antibodies and to goat anti–rabbit IgG antibodies (EnVision+, peroxidase; Dako) for polyclonal antibodies at 20°C for 45 minutes and rinsed with phosphate buffered saline (PBS) at pH 7.4. To visualize the peroxidase color reaction, sections were incubated with DAB-HCl solution (CB090; Dojin Chemicals, Tokyo; 50 mg dissolved in 100 mL of 0.05 M Tris-HCl buffer at pH 7.4) at 20°C for 10 minutes. Nuclear counterstaining was carried out with hematoxylin.

Transmission Electron Microscopy
For transmission electron microscopy, harvested tissues were resected by trimming (1.0 mm^3), fixed in 2.5% glutaraldehyde water solution for 2 hours, dehydrated with propylene oxide (Nakalai Tesque, Kyoto, Japan), and embedded in Epon 812 (Oken, Tokyo, Japan). In the final stage, ultrathin sections (100-nm thick) were prepared with an ultramicrotome (Ultracut N; Reihert, Wien, Austria), stained with 2% uranyl acetate (50% ethanol solution), and observed under a transmission electron microscope (H-700; Hitachi, Tokyo, Japan).

Cell Culture
Cultured PLL cells derived from the vicinity of OPLL plaque (named as "cultured OPLL cells") were isolated as described previously.[16] Briefly, the ligaments were harvested aseptically from the ossified tissue, minced into approximately 0.5-mm^3 pieces, and explanted onto a 100-mm diameter dish in 10 mL of Dulbecco's Modified Eagle Medium (#12320, Low Glucose 1X, lot 561521; GIBCO, Grand Island, NY) supplemented with 10% fetal bovine serum qualified (#1395965; GIBCO), 1% penicillin/streptomycin (#15140, 667553; GIBCO) at 37°C in a humidified atmosphere of 95% air/5% CO$_2$. The cultures were undisturbed for 48 hours, followed by replacement of the medium with an equal volume of fresh medium.

–671–
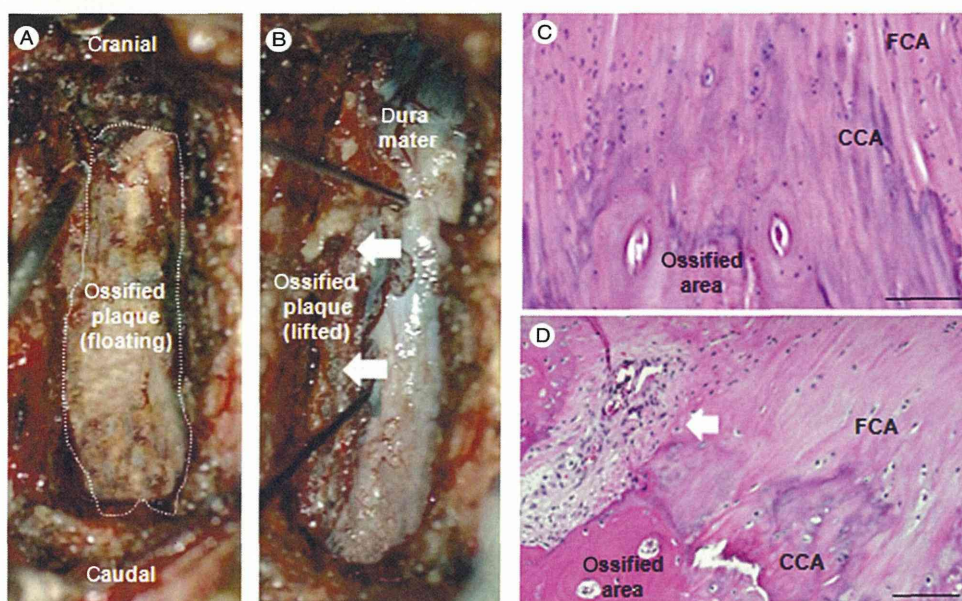
Figure 1. Intraoperative photographs taken during anterior floating and *en bloc* resection of the OPLL. The OPLL plaque was isolated circumferentially, like a floating "island" on the dura mater (**A**). After floating, the ossified plaque was lifted and extirpated from the dura mater (**B**). On hematoxylin and eosin staining, hypertrophic chondrocytes are present around the calcification front between the FCA and CCA (**C**). Note also the aggregation of mesenchymal cells (arrow) near the ossification area with blood vessel formation (**D**). (**C, D**): hematoxylin and eosin staining, scale bar = 100 μm). CCA indicates calcified cartilage area; FCA, fibrocartilage area; OPLL, ossification of the posterior longitudinal ligament.

The cells derived from the explants were harvested from the dishes with 0.02% ethylenediaminetetraacetic acid and 0.05% trypsin for further passages. The samples harvested from 6 patients without OPLL were cultured in a similar condition (named as "cultured non-OPLL cell").

Immunohistochemical Staining of Cultured Cells

For immunohistochemical staining with cultured cells, 2% paraformaldehyde was used for cell fixation at room temperature for 15 minutes after washing with PBS. The primary antibodies used in this study and in examination after cell fixation were as described previously (under the "Histological and Immunohistochemical Staining" section).

Immunoblot Analysis

To evaluate the expression levels of transcriptional factors, we used immunoblot analysis using the method described previously by our laboratory.[22] Briefly, the sample was solubilized in RIPA buffer, homogenized, and then stored at −80°C. The protein concentration was analyzed by the Bio-Rad DC protein assay kit (lot 500-0116; Bio-Rad Laboratories, Hercules, CA). Total protein (80 go/lane) was subjected to sodium dodecylsulfate polyacrylamide gel (15%) electrophoresis and transferred onto the polyvinylidene difluoride membrane in a semidry blot apparatus. The membranes were then washed twice in PBS, subsequently reacted with the primary antibodies (similar to those used in immunohistochemistry described earlier), and diluted overnight at 4°C sequentially by anti–rabbit IgG antibody and avidin-biotinylated peroxidase complex (1:200; EnVision System-HRP Labeled Polymer; Dako) for 3 hours. After triple washing in 0.1 M PBS, the membrane was immersed and then subjected to radiography to visualize the peroxidase activity and thus the level of antibody binding. To quantify the relative level of expression of 3 transcriptional factors in cultured OPLL and non-OPLL cells, we analyzed

the density of the bands on the photographic film with a densitometer using the NIH image analysis software (version 1.59/ppc; National Institutes of Health, Bethesda, MD). Data were expressed in relative values as semiquantitative data, representing the ratio of the density of each band to that of β-actin (1:500, rabbit IgG; Abcamn plc, Cambridge, England).

Statistical Analysis

Data are expressed as mean ± standard error of the mean. Differences between groups were examined by the Student t test. A P value of less than 5% was considered significant.

RESULTS

Histopathological Findings

The ossification front, comprising the fibrocartilage area (FCA), calcification front, and calcified cartilage area (CCA), was found close to the bony formation area (Figure 1C). The components exhibited irregular arrangement of features and extended longitudinally. The FCA also contained flat-shaped proliferating chondrocytes. A calcification front was noted along the line of ossification between the FCA and the CCA. Mature and hypertrophic chondrocytes forming a thick calcified cartilage layer in toluidine blue–stained sections were noted around the calcification front. The CCA raggedly extended longitudinally from the cartilage layer to the ossified area, and several hypertrophic chondrocytes were seen. At the abuttal region of the ossified area in the CCA, mesenchymal cells were found occasionally with small blood vessel formation (Figure 1D). These mesenchymal cells formed an island-like structure, and the initial ossification appeared to start from the border. In contrast, this layered structure was not seen in the control non-OPLL specimens. Instead, a thin, regular structure with a few chondrocyte was present.

Figure 2. On toluidine blue staining (**A**), the ossification of the posterior longitudinal ligament section shows layered structures from the FCA to the ossified area. Transmission electron microscopic examination shows hypertrophied chondrocytes (**B**) with nuclei surrounded by granular bodies and apoptotic chondrocytes (**C**) with flattened nuclei and cytoplasm in the CCA. (**A**) Toluidine blue staining (scale bar = 100 μm). (**B**, **C**) Transmission electron microscopy, (scale bar = 10 μm). CCA indicates calcified cartilage area; FCA, fibrocartilage area.
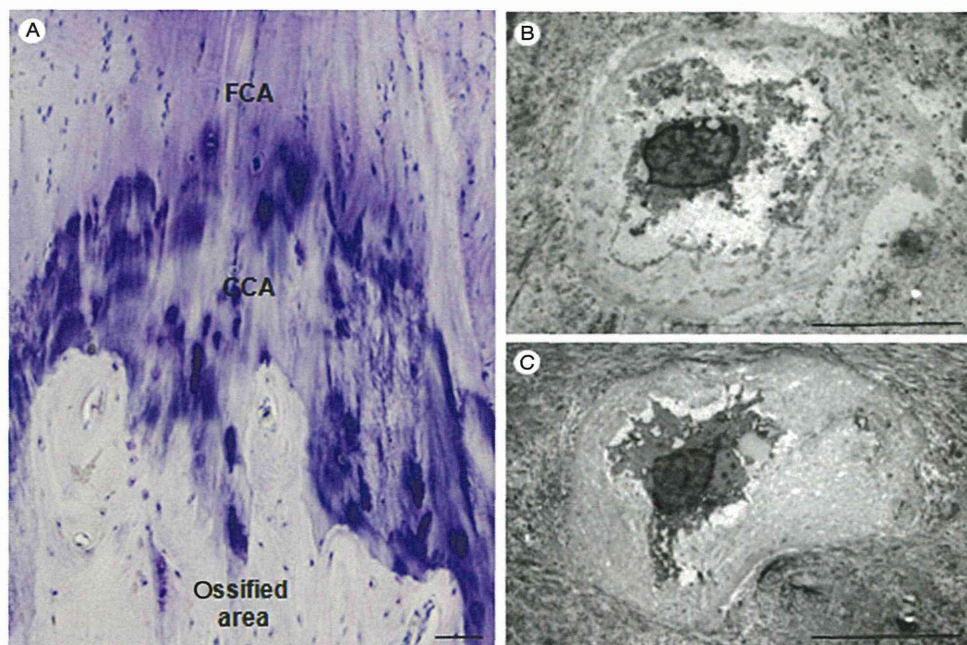
Transmission Electron Microscopic Findings in Chondrocytes

Hypertrophic chondrocytes were mainly evident in the CCA, especially near the calcification front (Figure 2A). The cytoplasm of these cells showed mature and hypertrophic changes, with abundant granular bodies surrounding the cell nucleus (Figure 2B). On the contrary, apoptotic chondrocytes, with cohesion of the cellular nucleus, were seen close to the ossified area in the CCA (Figure 2C). They were characterized by a flat cytoplasm and small-sized nuclei, which appeared flattened, containing clusters of granular bodies.
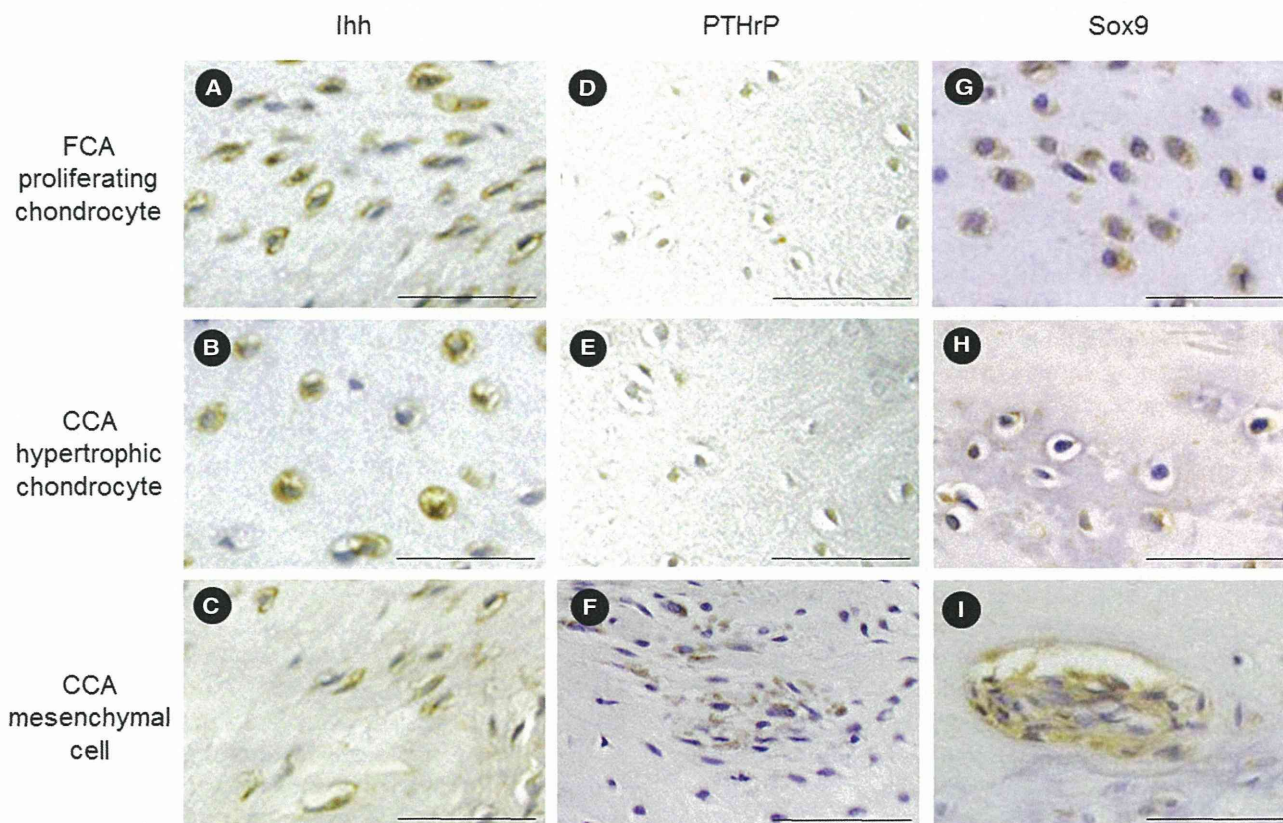
Figure 3. Immunohistochemical staining for Ihh (**A–C**), PTHrP (**D–F**), and Sox9 (**G–I**) in the ossification front: staining was strongly positive for Sox9 and Ihh in proliferating chondrocytes and was positive for PTHrP in hypertrophic chondrocytes. Staining for Sox9, Ihh, and PTHrP was positive in mesenchymal cells. CCA indicates calcified cartilage area; FCA, fibrocartilage area (scale bar = 100 μm).

type XI collagen   type X collagen   ALP
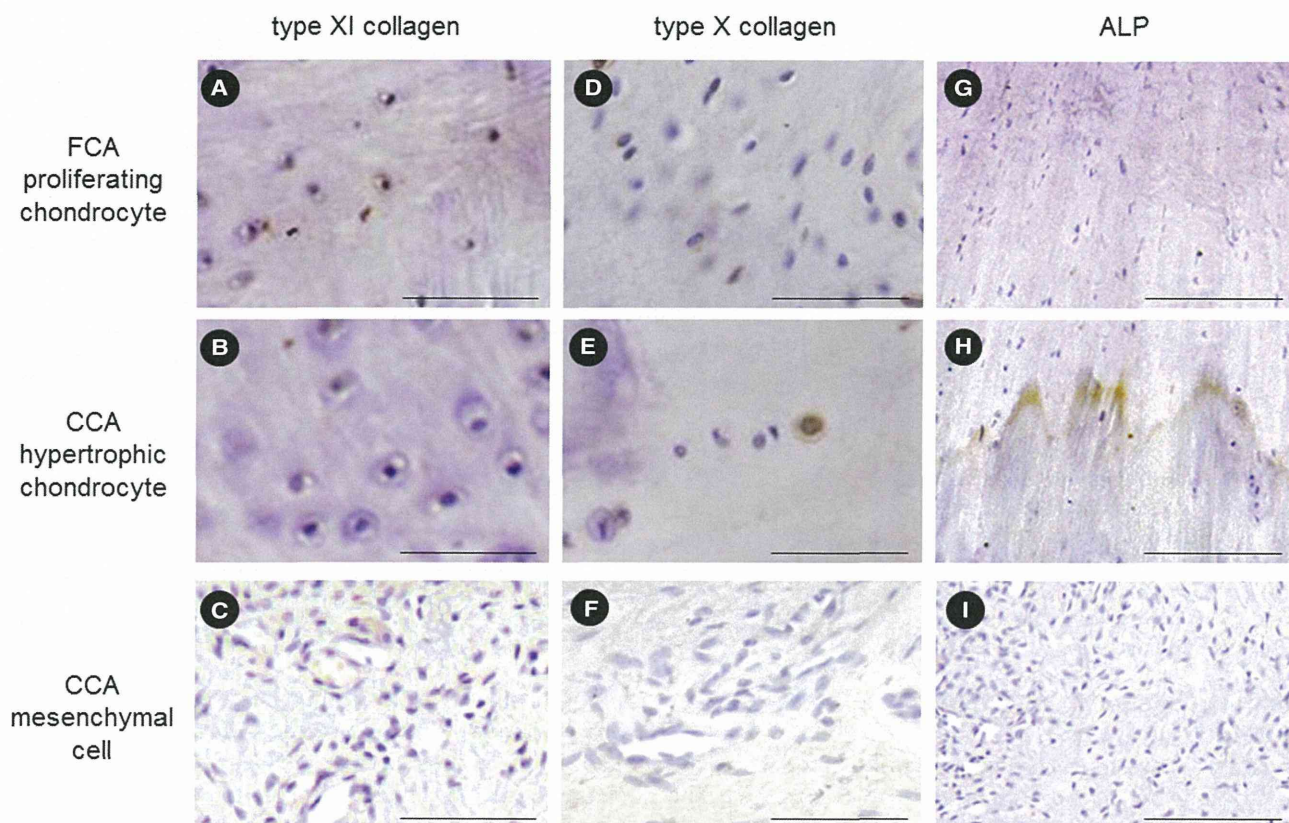
Figure 4. Immunohistochemical staining for type XI collagen (**A–C**), type X collagen (**D–F**), and alkaline phosphatase (**G-I**). Staining for type XI collagen was strongly positive in proliferating chondrocytes and was positive for type X collagen in hypertrophic chondrocytes. Staining for alkaline phosphatase was positive in hypertrophic chondrocytes in the CCA. CCA indicates calcified cartilage area; FCA, fibrocartilage area (scale bar = 100 μm).

Immunohistochemical Staining of Paraffin Section

Immunoreactivity to Ihh was noted in chondrocytes at various stages of differentiation but was particularly strong in proliferating chondrocytes in the FCA near the calcification front (Figure 3A–C; see Supplemental Digital Content Data 2, available at http://links.lww.com/BRS/A800). Staining for PTHrP was positive in proliferating chondrocytes and hypertrophic chondrocytes (Figure 3D–F). Immunoreactivity to Sox9 was noted in proliferating chondrocytes but not in hypertrophic chondrocytes (Figure 3G–I). Mesenchymal cells near the ossification area were immunopositive for Ihh, PTHrP, and Sox9. Proliferating chondrocytes, especially those in the FCA, were positive for type XI collagen (Figure 4A–C), whereas the hypertrophic chondrocytes both around the calcification front and in the CCA were positive for type X collagen (Figure 4D–F). Staining for ALP was noted in hypertrophic chondrocytes and chondroid matrix around the hypertrophic chondrocytes (Figure 4G–I). Immunopositive cells for these factors, such as Ihh, PTHrP, Sox9, type X collagens, and type XI collagens, were not present in the controlled samples, including ligamentous enthesis. Table 1 summarizes the results of immunohistochemical analysis.

Sox9, Ihh, and PTHrP Expression in Cultured OPLL Cells

The cultured OPLL cells exhibited a fibroblast-like, spindle-shaped appearance. The length of cultured cells ranged from 150 to 300 μm, and some cells had dendritic processes. There was no significant difference in appearance between cultured OPLL cells and non-OPLL cells, although the former type of cells tended to form multilayered structures compared with non-OPLL cells. Immunohistochemical staining showed expression of Ihh, PTHrP, and Sox9 in the cellular matrix of cultured OPLL cells (Figure 5). In contrast, non-OPLL cells were negative for Ihh, PTHrP, and Sox9.

Immunoblot Analysis

Figure 6 shows the results of immunoblot analysis for Ihh, PTHrP, and Sox9 in cultured OPLL cells. There were significant differences in the expression levels of these factors between cultured OPLL cells and non-OPLL cells: compared with the non-OPLL cells, the expression of Ihh (165%; $P < 0.05$), PTHrP (136%; $P < 0.05$), and Sox9 (182%; $P < 0.05$) was higher in cultured OPLL cells.

DISCUSSION

OPLL is characterized by an ectopic ossification that occurs in the PLL. In previously reported histological studies, the progression of OPLL was similar to enchondral ossification, which was regulated by cytokines, growth factors, transcriptional factors, or cell signaling.[10,11] These processes were coupled with cartilage development, involving chondrocyte differentiation. Enchondral ossification involves mesenchymal

TABLE 1. Summary of Immunohistochemical Staining of the Ossification Front of the Ossification of the Posterior Longitudinal Ligament

	Mesenchymal Cells (Near Ossified Area)	Hypertrophic Chondrocytes (CCA)	Proliferating Chondrocytes (FCA)	Fibroblasts (Fiber Area)
Sox9	+	−	++	−
Ihh	+	±	++	−
PTHrP	+	+	−	−
Col X	−	+	−	−
Col XI	−	−	+	−
ALP	−	+	−	−

Semiquantitative analysis conducted according to the method described by Song et al[40]: ++, strongly positive; +, moderately positive; ±, weakly positive; −, negative staining.

CCA indicates calcified cartilage area; FCA, fibrocartilage area.

cell condensation, aggregation, and differentiation into chondrocytes, followed by cell maturation, hypertrophy, calcification, and ultimately apoptotic cell death.[23–25] In the present study, the ossification front in OPLL included hypertrophic chondrocytes positive for type X collagen, a marker of hypertrophied chondrocytes,[26] and proliferating chondrocytes, which were positive for type XI collagen, a marker for chondrocyte maturation.[27] Although the exact role of these collagens in OPLL remains unclear, they are thought to play some roles in chondrocyte maturation and development of cartilage matrix, and genetic analysis showed involvement of these collagens in OPLL pathogenesis.[7,8] Alkaline phosphatase is also essential for the calcification process through the concentration of phosphate ions and is highly expressed in matrix vesicles secreted by hypertrophic chondrocytes.[28] Our study showed overexpression of growth factors and/or
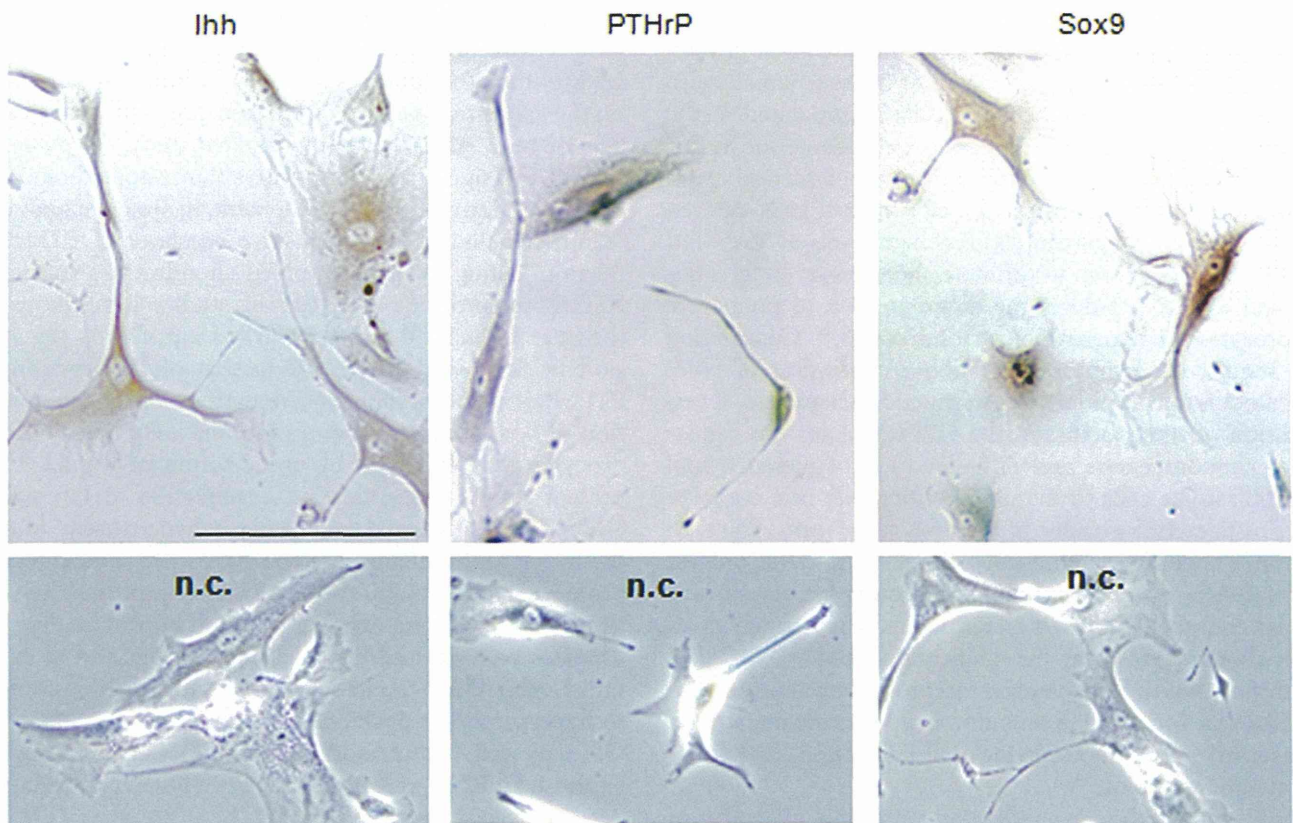
Figure 5. Representative immunohistochemical staining for Ihh, PTHrP, and Sox9 in cultured OPLL cells. Cellular matrix showed strong immunoreactivity. In contrast, control non-OPLL cells showed no immunoreactivity for these transcriptional factors. n.c. indicates normal control (scale bar = 100 μm).

−675−
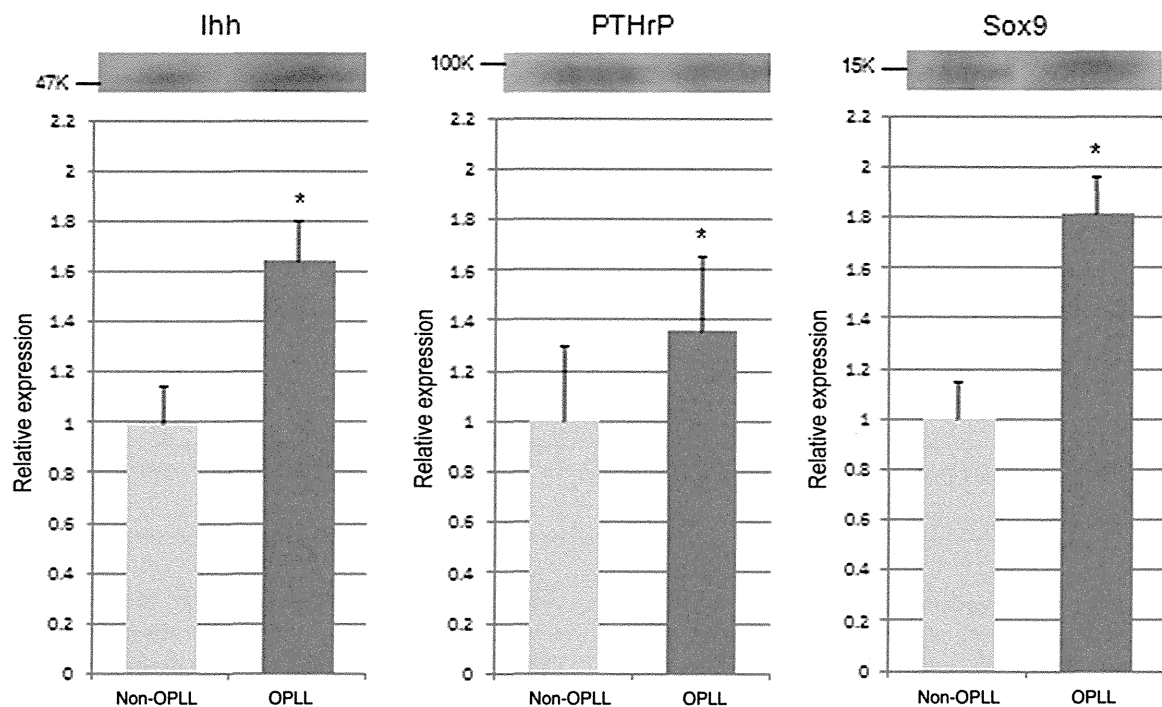
Figure 6. Immunoblot analysis of Ihh, PTHrP, and Sox9. The expression levels in cultured OPLL cells were significantly higher than those in non-OPLL cells. Data are mean ± SD. *P < 0.05.

changes in matrix constitution in OPLL, suggesting distur-bances of the aforementioned cell differentiation processes, leading to enchondral ossification.

The initiation of chondrocytes differentiation at the growth plate starts with the condensation of mesenchymal cells. In OPLL specimens, mesenchymal cells accumulated in the calcified cartilage layer with blood vessel formation. In our previous study using reverse-transcriptase polymersae chain reaction, we have demonstrated that cultured cells derived from ossified spinal ligament express high levels of Sox9 and Runx2.[15] Sox9 is known to promote chondrocyte differentia-tion, and Runx2 promotes the differentiation of premature chondrocytes to hypertrophic chondrocytes.[16] Considering these results, we hypothesize that overexpression of Sox9 and Runx2 is due to differences in genetic background. Over-expression of these factors in the OPLL violates the regula-tion of chondrogenesis and differentiation of mesenchymal or fibroblast-like cells to mature chondrocytes in a complex autocrine/paracrine manner. New blood vessel formation is an imperative factor for enchondral ossification, and this process is regulated by various cytokines and growth factors, such as vascular endothelial growth factor, which was strongly posi-tive in chondrocytes near the ossification front.[13,14] Vascular endothelial growth factor and its receptors were expressed on chondrocytes and acted in an autocrine/paracrine manner on neovascularization, mesenchymal cell infiltration, and chon-drocyte differentiation.[29,30]

With regard to chondrocyte hypertrophy, Ihh, a member of the Hedgehog family, is reported to be an essential factor for chondrocyte differentiation and is expressed on prehypertro-phic chondrocytes and acts in the surrounding tissues toward

the metaphysic tissues.[31-33] Ihh signaling is an imperative fac-tor for bone development in the embryo during postnatal development. The complete blocking of Ihh signaling will induce disturbances in the structures of the growth plate and lead to immature bone growth. There have been few reports on the expression pattern of Ihh signaling with respect to sex, age, or race. According to an in vitro study, the overexpres-sion of Ihh signaling could bring about ectopic bone forma-tion, or abnormal bone development, in systemic organs.[21,23]

Ihh signaling is also a positive regulator of PTHrP pro-duction, acting on hypertrophied chondrocytes through the PTHrP receptor.[11,19,30,34-37] Recent studies have shown that the interaction of Ihh and PTHrP is induced by the expres-sion of Sox9 and Runx2. Induction of Ihh signaling and PTHrP resulted in chondrocyte maturation under upregula-tion of Sox9, whereas maturation and calcification of chon-drocytes were inhibited by upregulation of Runx2.[38,39] The present results suggested that coactivation of Ihh signaling and PTHrP promoted chondrocyte hypertrophy, but once the hypertrophic change are complete in chondrocytes, the 2 proteins seem to inhibit the hypertrophy process. The present study showed strong expression of Ihh in proliferating chon-drocytes both around the calcification front and in cultured OPLL cells. These results suggest that Ihh signaling contribute to hypertrophy of proliferation chondrocytes in the FCA of OPLL as well as enchondral ossification. Furthermore, highly expressed mRNA of Ihh suggests gene-based abnormal chon-drogenesis in patients with OPLL.

We have demonstrated previously the presence of abnor-mal expression of Wnt/β-catenin signaling,[16] which regu-lates chondrocyte phenotype, maturation, and function in a